

# Structural Changes of 2D Fe<sub>x</sub>Mn<sub>1-x</sub>O<sub>2</sub> Nanosheets for Low-Temperature Growth of Carbon Nanotubes

Joohyun Lim,\* Xiaoyan Jin, Seong-Ju Hwang,\* and Christina Scheu

The synthesis of carbon nanotubes (CNTs) is usually done by metallic catalysts with a gaseous carbon precursor at high temperature. Yet, mild synthesis conditions can broaden the application of CNTs and their composites. In the present work, it is unraveled why partially substituted Fe ions in 2D MnO<sub>2</sub> nanosheets lead to the growth of CNTs at low temperatures of 400–500 °C. The local formation of Fe<sub>3</sub>C by carbon precursor explains the unusually high catalytic activity of 2D Fe<sub>x</sub>Mn<sub>1-x</sub>O<sub>2</sub> nanosheets for preparing CNTs. Finally, Fe<sub>3</sub>C is oxidized to Fe<sub>3</sub>C/FeO<sub>x</sub> yolk/shell morphology in ambient atmosphere after the CNT formation reaction. These results shed light on the development of novel catalyst materials that allow for efficiently prepare CNTs under mild conditions for their wider use in energy-harvesting applications.

## 1. Introduction

Carbon nanotubes (CNTs) are of great interest because of their superior mechanical, optical, thermal, electrical, magnetic, and chemical properties, not only as single material but also as composites with other functional materials.<sup>[1]</sup> More than several thousand tons of CNTs are being produced per year and are used in bicycle frames, battery electrodes, water filters, and so on.<sup>[2]</sup> For preparation of CNTs, chemical vapor deposition is regarded as the most facile and efficient method. Metals and metal carbides act as active catalysts to produce CNTs from gas phase carbon sources (e.g., methane and acetylene).<sup>[3,4]</sup> Using metal oxides as catalysts for CNTs are also reported, but in most cases, they were reduced to zero valent metals under reducing atmosphere. Determining the exact structure of the active catalyst is still one of the key questions, which is crucial for understanding and developing CNT-based materials.<sup>[5-7]</sup>

Recently, it was observed that 2D metal oxide nanosheets catalyzed CNT formation in mild condition of 400–500 °C, that is, much lower temperature than the typical reaction temperature of >700 °C.<sup>[8]</sup> Upon heat treatment in reducing atmosphere, 2D MnO<sub>2</sub> nanosheets are transformed into a 2D assembly of small-sized MnO nanoparticles showing unique catalytic property for CNT growth. The smaller crystal size of the catalyst possesses shorter carbon diffusion pathways for CNT formation.<sup>[3,9]</sup> The mild condition offers huge possibilities to prepare CNTs directly on fluorine-doped tin oxide electrode for photo(electro)chemical and solar-cell applications,<sup>[10,11]</sup> which suffers from low conductivity after high-temperature treatment.<sup>[12,13]</sup> Of prime importance is that partial Fe substitution within 2D MnO<sub>2</sub> nanosheets remarkably enhanced their catalytic activity for the CNT growth at 400 °C. However, the entire synthetic process and origin of catalytic activity of Fe<sub>x</sub>Mn<sub>1-x</sub>O<sub>2</sub> are not understood yet. Herein, we synthesize Fe-substituted 2D MnO<sub>2</sub> nanosheets (FMOs) with different amounts of Fe and study in depth their behavior as a catalyst for CNTs. The phase transformation of FMOs during CNTs formation and structure of active catalyst are studied using X-ray-based tools and electron microscopy.


## 2. Results and Discussion

### 2.1. Synthesis and Powder X-Ray Diffraction Analysis

FMOs were synthesized using the galvanic exchange reaction between Fe<sup>2+</sup> cations and 2D MnO<sub>2</sub> nanosheets.<sup>[14]</sup> Various amounts of Fe ions were introduced to MnO<sub>2</sub> nanosheets to examine their effect on the catalytic activity of FMOs. The overall oxidation states of Mn<sup>3+</sup>/Mn<sup>4+</sup> and Fe<sup>3+</sup> within the nanosheets were analyzed by X-ray absorption near-edge structure (XANES) spectroscopy, see Figure S1, Supporting Information. While the onset of the Fe K-edge remains the same with changing Fe content, an increase of Fe shifts the onset of the Mn K-edge toward higher energies, indicating a slight increase of Mn oxidation state upon Fe substitution. This is due to a stronger galvanic exchange reaction with increasing Fe content which leads to a replacement of more Mn<sup>3+</sup> with Fe<sup>3+</sup>. Accordingly, the Mn<sup>3+</sup>/Mn<sup>4+</sup> is lowered. Both Mn K-edge and Fe K-edge XANES spectra (Figure S1, Supporting Information) of all the investigated materials display small pre-edge peaks (denoted as P and P') corresponding to the dipole-forbidden

Dr. J. Lim, Prof. C. Scheu  
 Nanoanalytics and Interfaces  
 Max-Planck Institut für Eisenforschung GmbH  
 Max-Planck-Straße 1, Düsseldorf 40237, Germany  
 E-mail: j.lim@mpie.de

Dr. X. Jin, Prof. S.-J. Hwang  
 Department of Materials Science and Engineering  
 Yonsei University  
 Seoul 03722, Republic of Korea  
 E-mail: hwangsju@yonsei.ac.kr

 The ORCID identification number(s) for the author(s) of this article can be found under <https://doi.org/10.1002/adfm.202003849>.

© 2020 The Authors. Published by WILEY-VCH Verlag GmbH & Co. KGaA, Weinheim. This is an open access article under the terms of the Creative Commons Attribution License, which permits use, distribution and reproduction in any medium, provided the original work is properly cited.

DOI: 10.1002/adfm.202003849

1s → 3d transitions and also the main peak (denoted as C) related to the dipole-allowed 1s → 4p transition.<sup>[15–18]</sup> The increase of Fe content decreases the intensity of the resonance peak C for both Mn K-edge and Fe K-edge in the XANES data. Since the intensity of this peak reflects the local ordering around Mn/Fe ion, the observed lower intensity of this peak upon Fe substitution clearly demonstrates an increase of local structural disordering around Mn/Fe ion.<sup>[15]</sup> This finding can be ascribed to the diversification of local atomic arrangement around metal ions by enhancing the mixed distribution of MnO<sub>6</sub> and FeO<sub>6</sub> octahedra in the FMO lattices. Such an increase of structural disorder implies the lowering of lattice stabilization energy upon Fe substitution, which might facilitate the phase transformation of FMO during CNT growth.

FMOs were annealed in acetylene (C<sub>2</sub>H<sub>2</sub>) gas at 400 °C for 2 h. The products were denoted as FMO\_0–4 based on their overall Fe contents determined by energy dispersive X-ray spectroscopy (EDS) attached to a scanning electron microscope (SEM). The average Fe content is 0 (FMO\_0), ≈9 at% Fe (FMO\_1), ≈24 at% Fe (FMO\_2), ≈31 at% Fe (FMO\_3), and ≈54 at% (FMO\_4). The elements are homogeneously distributed at a microscopic scale (Figure S2, Supporting Information).

The effect of the annealing treatment in C<sub>2</sub>H<sub>2</sub> atmosphere as well as the Fe content on the crystal structure of FMOs were investigated with powder X-ray diffraction (XRD) (Figure 1a). It is important to mention that the FMO before annealing in C<sub>2</sub>H<sub>2</sub> has an MnO<sub>2</sub> crystal structure.<sup>[14]</sup> Most FMO\_0 peaks in the XRD pattern are assigned to an orthorhombic Mn<sub>3</sub>O<sub>4</sub> phase. FMO\_0 shows additional strong peaks which correspond to the (111), (200), and (220) reflections of a cubic MnO phase. The phase transformation from the initial MnO<sub>2</sub> nanosheet to Mn<sub>3</sub>O<sub>4</sub>/MnO is related to the reduction of Mn ions during the reaction with C<sub>2</sub>H<sub>2</sub>. All the FMO\_1–4 samples display similar XRD peaks, which can be assigned to both the Mn<sub>3</sub>O<sub>4</sub> and MnFe<sub>2</sub>O<sub>4</sub> phases. The formation of MnFe<sub>2</sub>O<sub>4</sub> phases is due to the presence of Fe

ions in the materials. There are no strong peaks of the MnO phase in these materials, strongly suggesting a limited crystal growth and depressed reduction of MnO<sub>x</sub> by the Fe substitution.<sup>[14]</sup> Broad peaks of CNTs, that is, (001) and (002) are found in FMO\_3 and FMO\_4, highlighting the low crystalline nature of CNTs formed in FMOs with higher Fe contents.

## 2.2. XANES Spectroscopic Analysis

The oxidation state and local symmetry of Fe and Mn species in FMOs were analyzed with XANES. The overall shape of several main peaks (denoted as A, B, and C) and edge position of Fe K-edge XANES spectra are similar for FMOs and reference Fe<sub>2</sub>O<sub>3</sub>, indicating the trivalent Fe<sup>3+</sup> oxidation state of FMOs (Figure 1b). This finding clearly demonstrates that FMOs contain Fe<sub>2</sub>O<sub>3</sub> and/or the MnFe<sub>2</sub>O<sub>4</sub> with Fe<sup>3+</sup> oxidation state. A small pre-edge peak (denoted P) is found in Fe K-edge XANES spectra of FMOs, presenting the 1s to 3d transition. This transition is forbidden by an electronic dipolar selection rule but can be partially allowed in the case of a quadrupole-allowed transition or a mixing of 4p and 3d states in the tetrahedral symmetry.<sup>[15–18]</sup> A weak pre-edge peak in FMOs provides strong evidence for the octahedral symmetry of Fe species in the structures. The Mn K-edge spectra of FMOs display similar shape and edge position to those of Mn<sub>3</sub>O<sub>4</sub> reference (Figure 1c), reflecting mixed Mn<sup>2+</sup> and Mn<sup>3+</sup> oxidation states of FMOs. A weak pre-edge peak in Mn K-edge XANES spectra of FMOs also confirms the octahedral symmetry of Mn ion in FMOs.<sup>[19]</sup>

## 2.3. Electron Microscopy Analysis

To verify the structure of FMOs with the evolution of CNTs, SEM, and transmission electron microscopy (TEM) images of

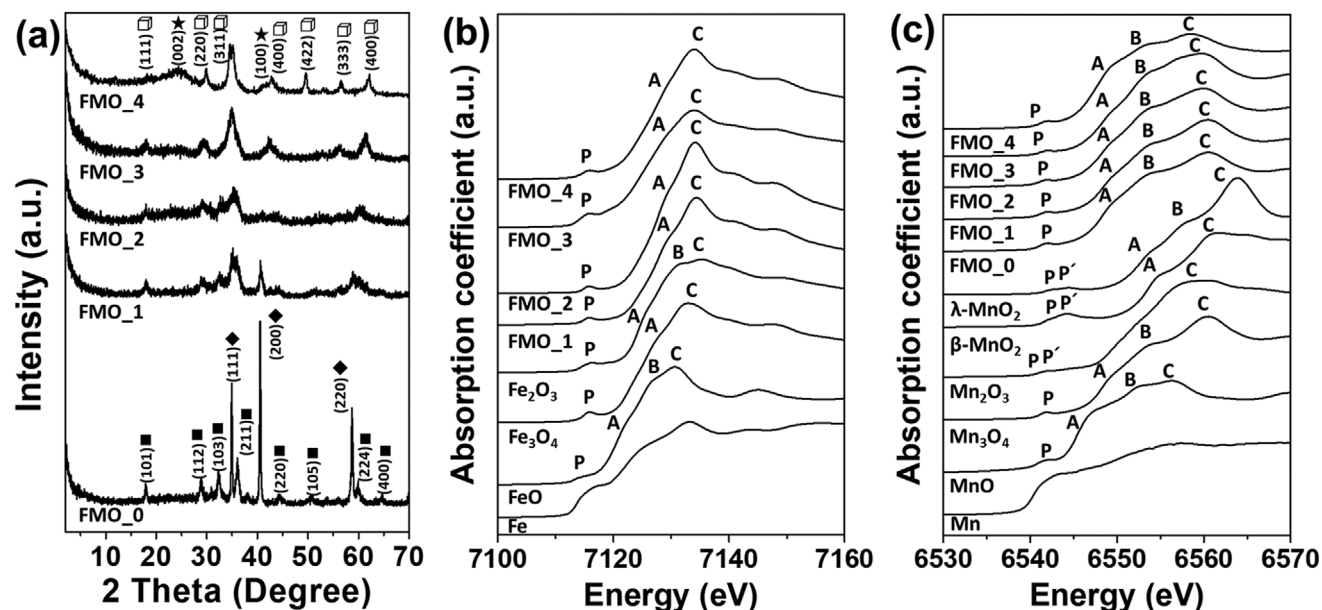


**Figure 1.** a) XRD patterns of FMOs. Reflections of Mn<sub>3</sub>O<sub>4</sub>, MnO, MnFe<sub>2</sub>O<sub>4</sub>, and CNTs are denoted as squares, diamonds, cubes, and stars, respectively. b) Fe K-edge and c) Mn K-edge XANES spectra of FMOs as compared with reference spectra of elemental Fe/Mn or Fe/Mn oxides.

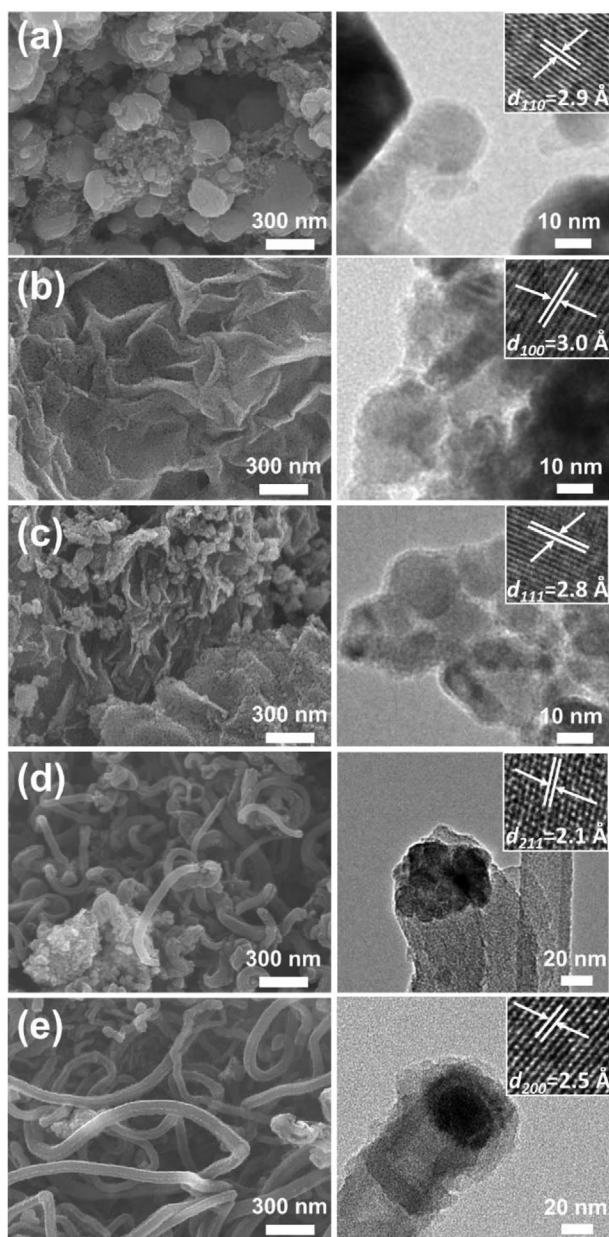


**Figure 2.** SEM and TEM images of a) FMO\_0, b) FMO\_1, c) FMO\_2, d) FMO\_3, and e) FMO\_4. Insets show lattice distances of individual particles, which are related to  $\text{Mn}_3\text{O}_4$ ,  $\text{MnFe}_2\text{O}_4$ , or  $\text{Fe}_3\text{C}$ .

FMOs were acquired. As presented in **Figure 2a**, the FMO\_0 consists of bigger and smaller crystalline particles coated with thin carbon layers. The lattice distance from the small particles is assigned to (110) of the  $\text{Mn}_3\text{O}_4$  in accordance with XRD result (inset in **Figure 2a**). Both FMO\_1 and FMO\_2 show smaller interconnected particles in 2D assemblies due to the presence of Fe ions preventing crystal growth<sup>[14]</sup> of  $\text{MnO}_x$  matrix (**Figure 2b,c**). The carbon-coated small particles of FMO\_1 and FMO\_2 are assigned to the (110) and (111) planes of the  $\text{Mn}_3\text{O}_4$ , respectively. The growth of CNTs is observed for FMO\_3 and FMO\_4. FMO\_4 displays the formation of longer and thicker CNTs than FMO\_3, underscoring the important role of Fe substituent ion in CNT

growth (**Figure 2d,e**). The 2D assemblies are still attached to CNTs, strongly suggesting the growth of CNTs from these 2D assemblies (**Figure S3**, Supporting Information).

Crystal particles detached from 2D assemblies are still present at the head part of CNTs, demonstrating a tip-growth mechanism of CNTs (**Figure 2d,e**).<sup>[20]</sup> The crystal planes in FMO\_3 can be assigned not only to (400) of  $\text{MnFe}_2\text{O}_4$  but also to (211) of an orthorhombic  $\text{Fe}_3\text{C}$ . In FMO\_4 lattice, distances corresponding to (112) of  $\text{Mn}_3\text{O}_4$ , (222) of  $\text{MnFe}_2\text{O}_4$ , and (200) of  $\text{Fe}_3\text{C}$  are found. Using the presented synthetic method, CNTs can be obtained within a very short reaction time of 30 min but not without  $\text{C}_2\text{H}_2$  (**Figure S4a,b**, Supporting Information). Longer CNTs are prepared by employing a higher temperature of 500 °C and longer reaction time of 20 h (**Figure S4c**, Supporting Information). These results emphasize that the Fe substitution as well as the control of reaction time and reaction temperature are essential for the efficient growth of CNTs from FMOs.

For comparison, Sn-substituted  $\text{MnO}_2$  nanosheets (SMOs) were also prepared to examine the importance of Fe for CNT growth at low temperature.<sup>[14]</sup> SMOs were annealed in  $\text{C}_2\text{H}_2$  gas at 400 °C for 2 h. The products were denoted as SMO\_0–2, which have an average Sn content of 0 (SMO\_0),  $\approx 9\%$  Sn (SMO\_1), and  $\approx 39\%$  Sn (SMO\_2). The elements are homogeneously distributed at a microscopic scale (**Figure S5**, Supporting Information). Similar to Fe, Sn induces a phase transformation of nanosheets to  $\text{SnMn}_2\text{O}_4$  phases suppressing the formation of  $\text{MnO}_x$  crystals (**Figure S6**, Supporting Information). However, all SMOs do not catalyze the formation of CNTs, strongly confirming the unique role of Fe for CNT growth at low temperature (**Figure S7**, Supporting Information).

#### 2.4. Local X-Ray Dispersive Spectroscopy Analysis

To unravel the structure of active catalyst which promotes CNT growth, local investigation of the corresponding FMO particles is indispensable. First, the changes in chemical composition of the FMOs were analyzed using high angle annular dark field (HAADF) and EDS in scanning TEM (STEM) mode (**Figure 3** and **Table 1**). FMOs are composed of interconnected particles in 2D assemblies coated with carbon. Particles in the tip of short CNTs ( $< \approx 1 \mu\text{m}$ ) and long CNTs ( $> \approx 1 \mu\text{m}$ ) are detached from the assembled region. The 2D assemblies have a homogeneous distribution of Fe, Mn, O, and C elements (**Figure 3a**). The particles on the top of short CNTs show a higher Fe content than the 2D assemblies and a higher Fe than Mn content (**Figure 3b**). For particles attached to long CNTs, Fe signal appears only in the core part whereas O signal is discernible for entire parts of particles, strongly suggesting a core/shell morphology without the presence of Mn (**Figure 3c**). The increase of the total Fe content in FMO\_0 to FMO\_4 leads to the elongation of CNT, confirming the major role of Fe ion and negligible role of Mn ion for catalyzing the growth of CNT.

#### 2.5. Electron Energy Loss Spectroscopy Analysis

Electron energy loss spectroscopy (EELS) was conducted in STEM mode to further investigate the chemical composition of

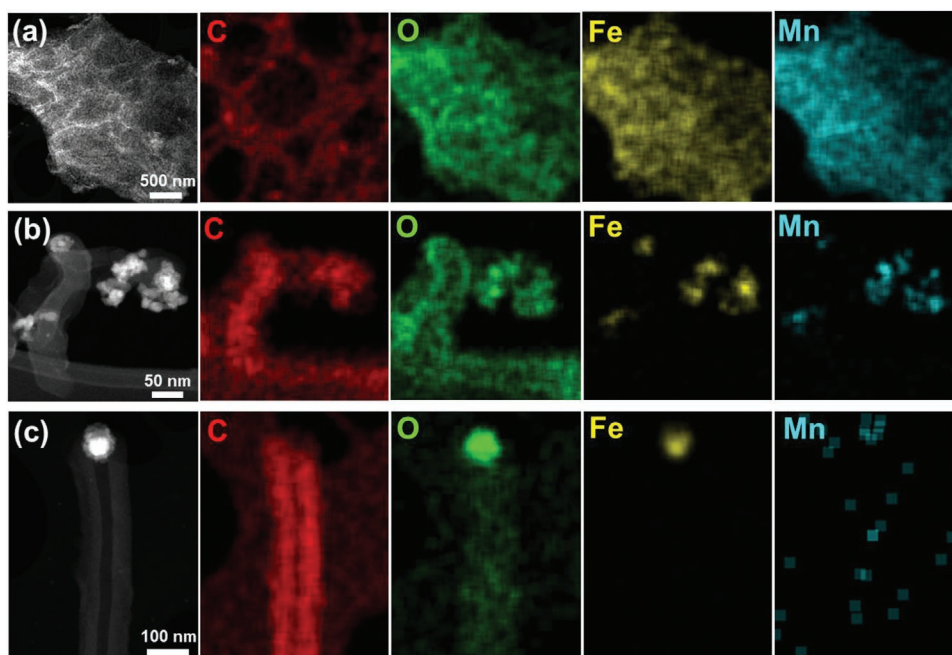


**Figure 3.** HAADF-STEM images and STEM-EDS maps of a) 2D assemblies, b) short CNT, and c) long CNT regions.

FMOs. **Figure 4a** displays the core loss EELS data in the energy loss regime from 600 to 740 eV for 2D assemblies, short CNT, and long CNT, respectively. In this energy loss regime, the Mn  $L_{2,3}$ - and Fe  $L_{2,3}$ -edges occur and the energy loss near-edge structure (ELNES) of each of these element specific edges shows the typical white lines of transition metals in accordance with the literature.<sup>[21,22]</sup> The intensity of the Mn  $L_{2,3}$ -edge is highest in the 2D assemblies, low in the short CNT, and not detected above the noise level in the long CNT. The relative amount of Mn and Fe can be obtained from the edge intensity in the core loss EELS data combined with the low loss spectra to remove plural scattering contributions. The calculated ratio of Mn:Fe is 58:42, 39: 61, and 0:100 for 2D assemblies, short CNT, and long CNT, respectively, confirming the key role of Fe for CNT growth. The intensity of the Fe  $L_{2,3}$ - and Mn  $L_{2,3}$ -edges were also used to visualize the elemental distribution within these morphologies. The maps are shown in Figure 4b–d together with the corresponding ADF-STEM image. Both Fe and Mn

elemental maps reveal a similar, homogeneous distribution of the elements in the entire monitored area of the 2D assemblies (Figure 4b). While Fe is homogeneously distributed in the catalyst particle of the short CNT, Mn is concentrated only in the core of the particle (Figure 4c). This is due to the higher reactivity of Fe species with carbon source than Mn species. Figure 4d shows that Mn is not present in the catalyst particles of the long CNT besides their core/shell morphology. This is further discussed later.

## 2.6. Detailed EELS Analysis

ELNES was analyzed in detail to further investigate the structural changes of FMOs. All the regions display  $\pi^*$  and  $\sigma^*$  peaks at C K-edge (**Figure 5a**). Because the  $\pi^*$  peak corresponds to  $sp^2$  bonding, the weak  $\pi^*$  peak in the 2D assemblies represents amorphous carbon layers whereas pronounced  $\pi^*$  peaks in both short CNT and long CNT regions verify graphitic CNT.<sup>[23]</sup> ELNES spectra of Fe  $L_{2,3}$ - and Mn  $L_{2,3}$ -edges exhibit two white lines whose ratio provides a sensitive probe to the oxidation state of the transition metal ion (Figure 5b–d and Table 1). The higher intensity ratio of  $I(L_3)/I(L_2)$  reflects the lower oxidation state of Fe- and Mn-based oxides.<sup>[21,22]</sup> Both 2D assemblies and short CNT regions display similar  $I(L_3)/I(L_2)_{Fe}$  values of  $\approx 5.2$ , which is larger than that of long CNT region ( $\approx 4.4$ ). The number of  $Fe^{3+}$  ions from the entire Fe species can be estimated using the following equation.

$$I(L_3)/I(L_2)_{Fe} = 1/(ax^2 + bx + c) - 1 \quad (1)$$

where  $a = 0.18 \pm 0.01$ ,  $b = -0.46 \pm 0.02$ ,  $c = 0.368 \pm 0.005$ , and  $x = Fe^{3+}/\Sigma Fe$ .<sup>[21]</sup> The relative  $Fe^{3+}$  amount is lower in long CNT region ( $\approx 44\%$ ) than in 2D assemblies and short CNT regions ( $\approx 58\%$ ),

**Table 1.** Chemical content obtained from STEM-EDS, intensity ratio of Fe  $L_{2,3}$ -edge, calculated  $Fe^{3+}/\Sigma Fe$  ratio, and intensity ratio of Mn  $L_{2,3}$ -edge from EELS spectra.

	2D assemblies	Short CNTs	Long CNTs		
			Entire	Core	Shell
Fe [at%]	20.0	41.2	100.0	100.0	100.0
Mn [at%]	80.0	58.8	—	—	—
Fe	5.2	5.2	4.4	3.3	4.0
$I(L_3)/I(L_2)_{Fe}$					
$Fe^{3+}/\Sigma Fe$ [%]	58	58	44	33	49
Mn	3.2	3.2	—	—	—
$I(L_3)/I(L_2)_{Mn}$					

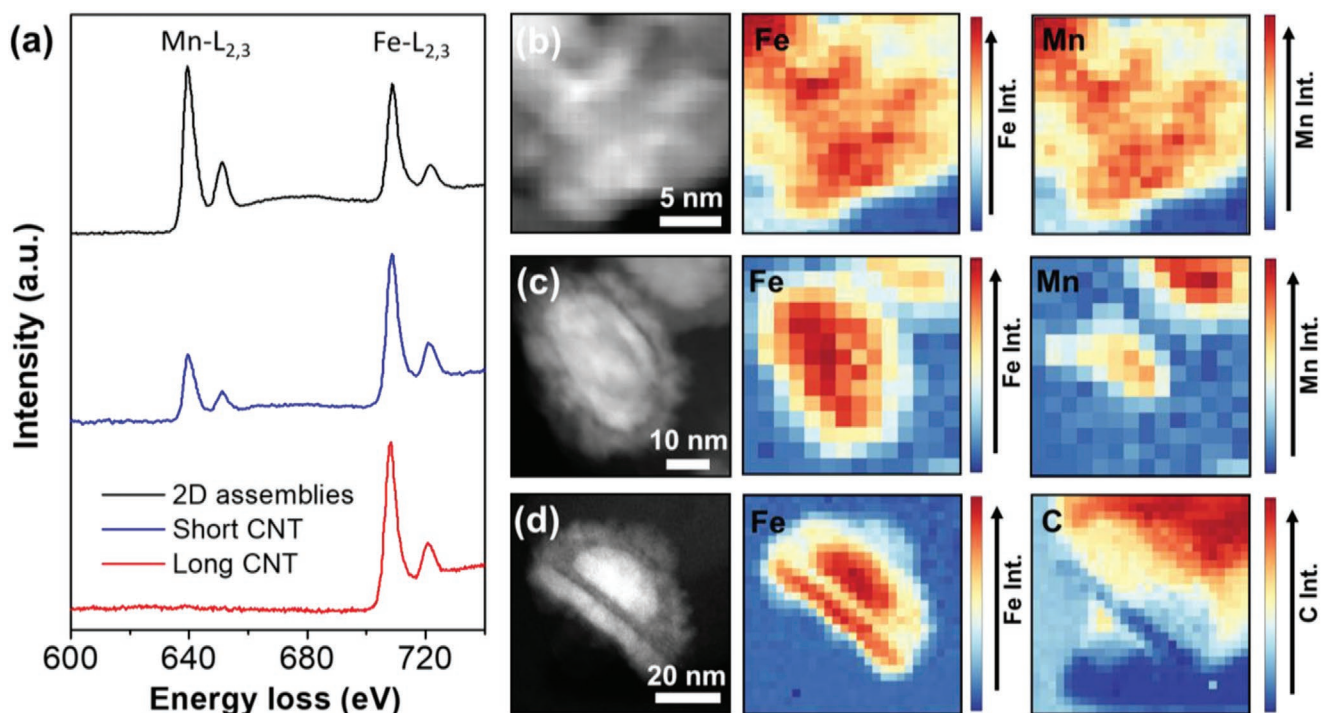


**Figure 4.** a) Core loss ELNES spectra of Mn  $L_{2,3}$ - and Fe  $L_{2,3}$ -edges. ADF-STEM and core loss intensity distribution maps of b) 2D assemblies, c) short CNTs, and d) long CNTs.

indicating a more reduced state of Fe species on the top of a long CNT (Table 1 and Figure 5c). Both the aggregated assemblies and short CNT regions show similar  $I(L_3)/I(L_2)_{Mn}$  ratio of  $\approx 3.2$ , which is obviously different from those of MnO ( $\approx 4.0$ ) and  $Mn_2O_3$  ( $\approx 2.5$ ).<sup>[22]</sup> These results clearly demonstrate that the Mn species in these regions have mixed  $Mn^{2+}/Mn^{3+}$  oxidation states, which is in accordance with the XRD and XANES results.

The O K-edges ELNES spectra of all the regions show characteristic pre-edge peaks at  $\approx 529$  eV corresponding to transitions from 1s state to unoccupied hybrid states of oxygen 2p and transition metal 3d orbitals (Figure 5e).<sup>[24]</sup> This result demonstrates the existence of Fe- and Mn-based oxides in all the regions under investigation.

ADF-STEM image of particles on the head of long CNTs exhibits a core/shell morphology (Figure 6a). The core has a brighter intensity than shell which is composed of tiny particles. There is an empty space between core and shell, clarifying the yolk/shell morphology of these particles. ELNES maps were taken to obtain elemental distributions around the yolk/shell (Figure 6a). Carbon is present in yolk/shell as well as CNT region, as evidenced by C K-map. Fe L- and O K-edge ELNES maps show a more intense Fe signal from the core while the highest O signal stems from the shell, indicating that the shell is  $FeO_x$  but the core is in metallic state. C K-edge ELNES spectrum from CNT area presents strong  $\pi^*$  peak related to  $sp^2$  bonding of graphitic carbon (Figure 6b). The  $\pi^*$  peak from shell area is weaker due to the initial amorphous carbon shell covering the particles in this area. The strong  $\pi^*$  peak from core area is interpreted as the characteristic of carbon atoms in iron carbides.<sup>[23,25]</sup> The asymmetric Fe  $L_{2,3}$ -edges ELNES spectral feature from core area also suggests the existence of iron carbide phases (Figure 6c).<sup>[23,25]</sup> These iron carbides can be

formed by the reaction with  $C_2H_2$  gas under reduction condition. The core has a lower  $Fe^{3+}/\Sigma Fe$  value than does the shell, confirming the presence of Fe species as iron carbide phase (Figure 6c and Table 1). The iron carbide core is supposed to be  $Fe_3C$ , because it is the most thermodynamically favorable phase among many iron carbide phases. However, even for  $Fe_3C$ , the formation of this carbide phase is unfavorable in the range of 400 and 450 °C ( $\Delta G^\circ = 22\,500 - 18.4T(J)$ ).<sup>[26]</sup> Also, a recent in situ TEM study reported that formation of CNT using  $Fe_3C$  needed a higher onset temperature ( $\approx 800$  °C).<sup>[5]</sup> This fact implies that highly exposed Fe ions on the thin layer of 2D nanosheets employed in this study play a crucial role in providing a faster mobility and a higher reactivity toward the  $Fe_3C$  formation than other metal oxide nanostructures. Additionally, the increased structural disorder of FMOs upon Fe substitution results in the lowering of lattice stabilization energy, which is effective in promoting the phase transformation into the  $Fe_3C$  phase. The oxide shell is formed in ambient atmosphere after completing the growth reaction of CNT, because  $Fe_3C$  is unstable especially below 750 °C.<sup>[27]</sup> The formation of  $Fe_3C/FeO_x$  yolk/shell structure can be understood in terms of different diffusion rates of the elements, that is, Kirkendall effect.<sup>[28]</sup> The phase segregation into Mn-free  $Fe_3C$  can be explained by the fact that  $Mn_3C$  is thermodynamically less stable than  $Fe_3C$  (especially below 850 °C) and this phase can exist only in the temperature range of 950–1050 °C.<sup>[29,30]</sup>

## 2.7. 3D Electron Tomography

The full 3D morphology of the crystalline particles attached to the head of long CNTs was investigated using electron

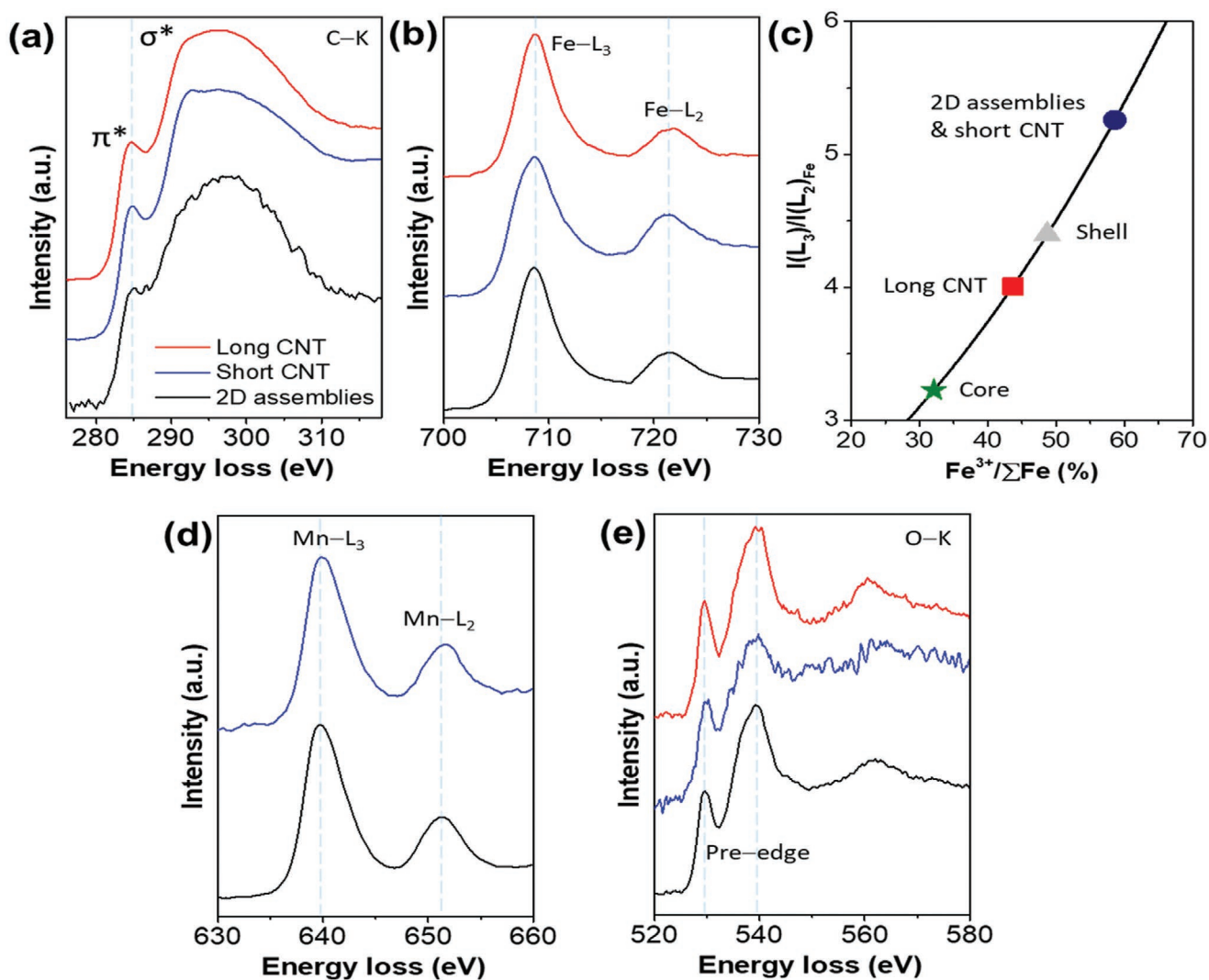


Figure 5. Core loss ELNES spectra of a) C K-, b) Fe L<sub>2,3</sub>-, d) Mn L<sub>2,3</sub>-, and e) O K-edges. c) Plot of the  $I(L_3)/I(L_2)_{Fe}$  intensity ratio versus relative Fe<sup>3+</sup> content.

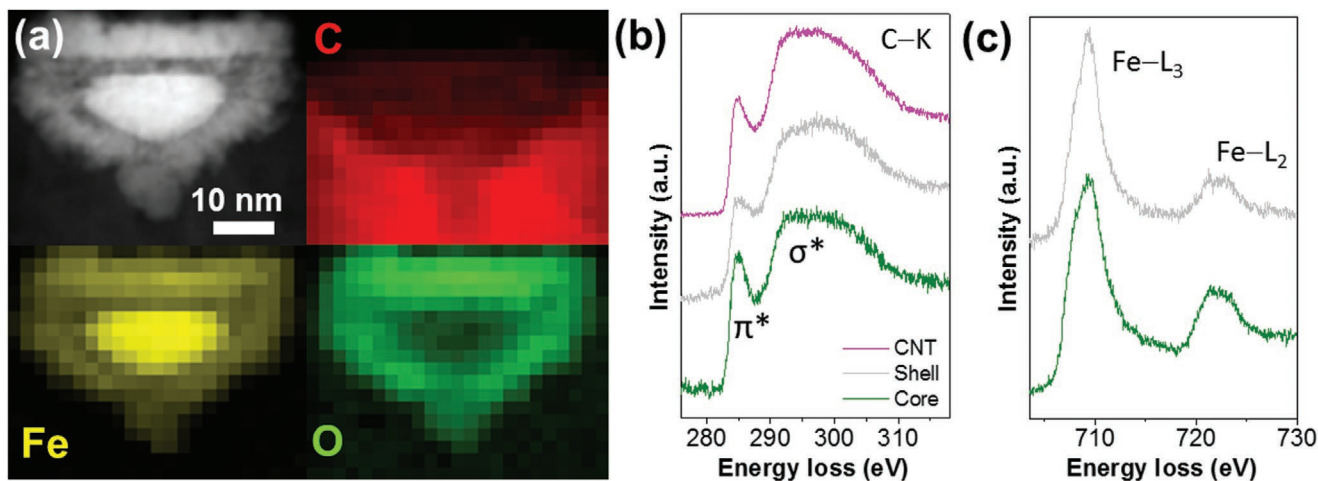


Figure 6. a) ADF-STEM image and elemental maps of C, Fe, and O. b) C K-, and c) Fe L<sub>2,3</sub>-edge ELNES spectra for the head of a long CNT region.

tomography. First low magnification tomogram shows a bright particle at the head of CNT (**Figure 7A**). The morphology was reconstructed using a tilt series of HAADF-STEM images obtained in the range of  $\pm 60^\circ$  in  $5^\circ$  steps (**Figure 7Aa–c**). The particle (yellow) in reconstructed volume is entirely covered by carbon (purple) grown as 1D CNT (**Figure 7Ad–f** and **Movies S1** and **S2**, Supporting Information). This result supports that the mechanism responsible for the CNT formation begins with a carbon layer formation around FMO crystal grains expelling the Mn species, and then the CNT growth follows. To visualize 3D morphology of the yolk/shell morphology of the head particles, another reconstruction was performed where the contrast setting was changed for visualization (**Figure 7Ba–c**). A yellow core particle is surrounded by gray empty area, separating the core and outer shell (**Figure 7Bd** and **Movie S3**, Supporting Information), verifying the yolk/shell morphology of  $\text{Fe}_3\text{C}/\text{FeO}_x$ .

The reaction mechanism of FMOs with  $\text{C}_2\text{H}_2$  is illustrated in **Figure 8**. With elevating reaction temperature under  $\text{C}_2\text{H}_2$  flow, 2D nanosheets start to get reduced to form small crystal grains coated with amorphous carbon layers. Homogeneously dispersed Fe ions in  $\text{MnO}_2$  are migrated to form  $\text{Fe}_3\text{C}$  phase. As evidenced by Fe K-edge XANES analysis, enhancement of

structural disorder around Fe ion with the increase of Fe content promotes the formation of  $\text{Fe}_3\text{C}$  phase during the reaction with  $\text{C}_2\text{H}_2$ . High carbon solubility and catalytic activity of  $\text{Fe}_3\text{C}$  are responsible for the CNT formation via the tip-growth mechanism,<sup>[20]</sup> where the catalyst particles are detached from the main 2D assemblies during CNT growth. After completing the reaction, the outer shell of  $\text{Fe}_3\text{C}$  grains is oxidized to  $\text{Fe}_3\text{C}/\text{FeO}_x$  yolk/shell morphology due to the different diffusion rates of elements.

### 3. Conclusion

This work has shed light on the structural change of partially Fe-substituted 2D  $\text{Fe}_x\text{Mn}_{1-x}\text{O}_2$  nanosheets for CNT growth at low temperature. The effects of Fe content, reaction temperature, and reaction time on the efficiency of CNT growth were investigated. The reaction with gaseous carbon precursor induces the formation of  $\text{Fe}_3\text{C}$  particles from  $\text{Fe}_x\text{Mn}_{1-x}\text{O}_2$  nanosheets, which have an unusually high catalytic activity for the formation of CNT. After the reaction, the  $\text{Fe}_3\text{C}$  is oxidized to form  $\text{Fe}_3\text{C}/\text{FeO}_x$  yolk/shell morphology. Since the catalytic properties for CNT growth are strongly dependent on the structure of the catalyst,

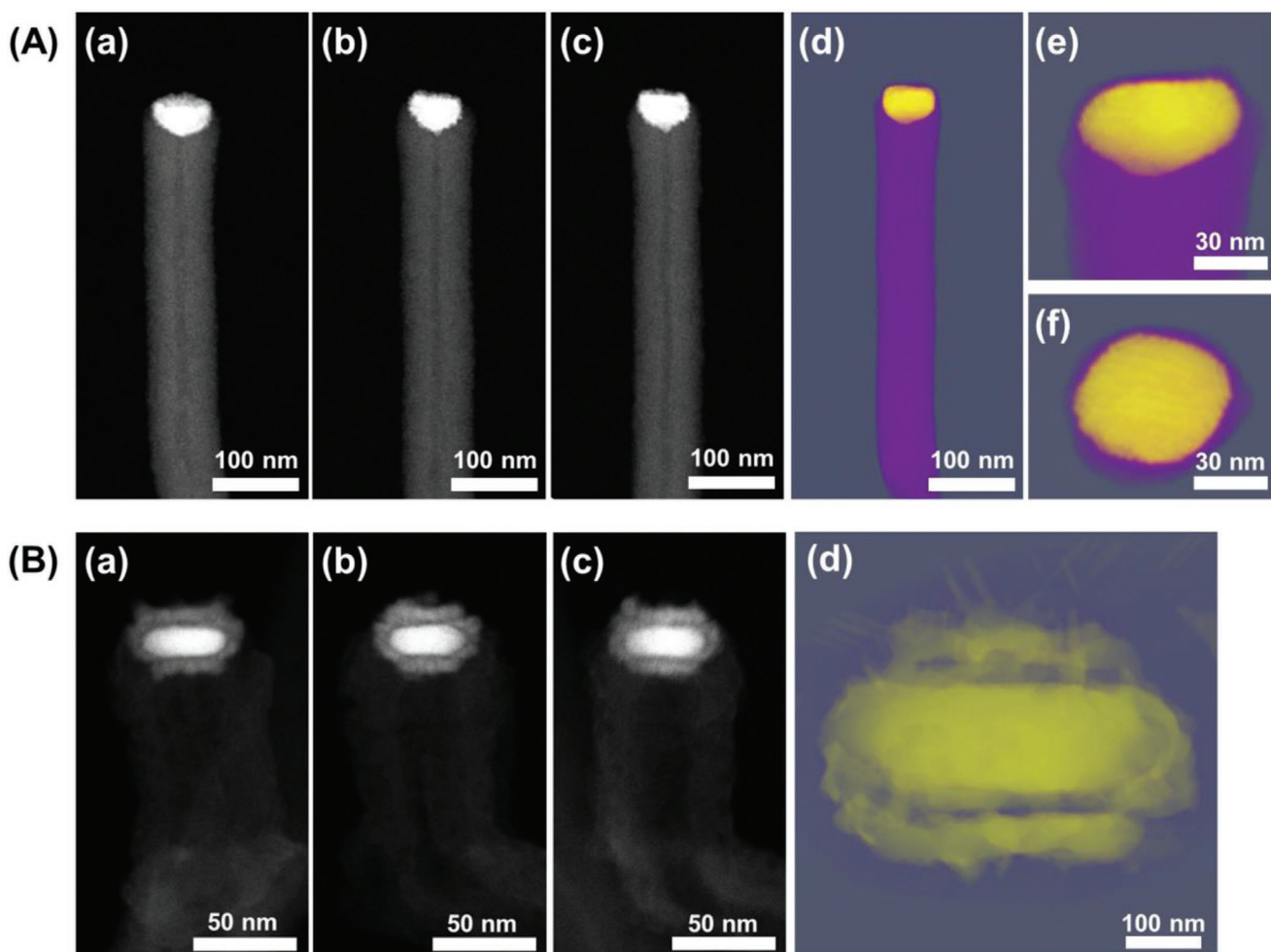


**Figure 7.** HAADF-STEM images from a) 0, b)  $-60^\circ$ , and c)  $+60^\circ$  tilt angle of a particle in a long CNT. d) Reconstructed volume and e) side- and f) top-viewed images. Row A and row B differ in the settings of the contrast to visualize (A) the whole CNT or (B) the yolk/shell particle more clearly.

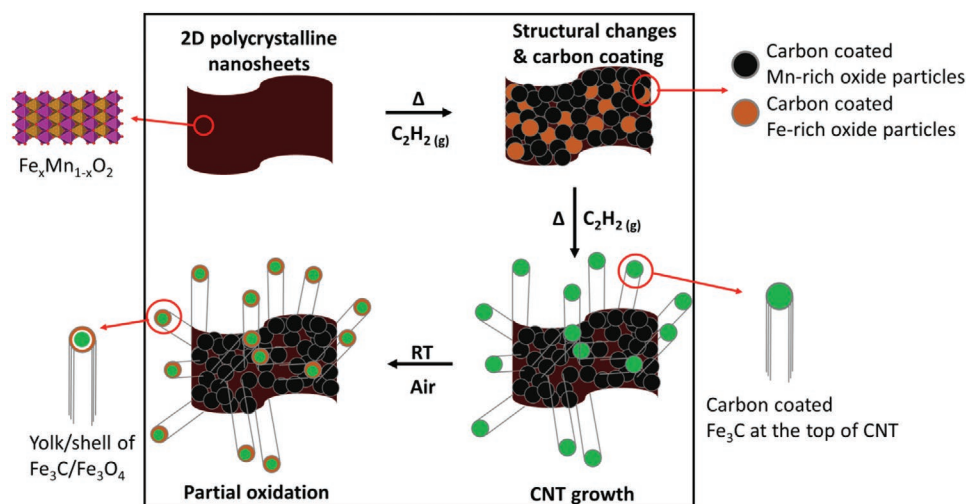


**Figure 8.** Schematic drawing illustrating the mechanism for structural changes of the FMO during CNT growth at low temperature.

it is evident that optimization of the catalyst requires detailed structural studies using electron microscopy techniques.

#### 4. Experimental Section

**Synthesis:** 2D  $\text{MnO}_2$  nanosheets were prepared by chemical oxidation of  $\text{Mn}^{2+}$  ion with the help of hydrogen peroxide.<sup>[31]</sup> Fe ion was introduced into the  $\text{MnO}_2$  nanosheets using galvanic exchange reaction,<sup>[14]</sup> and annealed at  $400^\circ\text{C}$  for 2 h under  $\text{C}_2\text{H}_2/\text{Ar}$  mixture gas flow ( $\text{C}_2\text{H}_2:\text{Ar} = 100:5$ ).

**X-Ray Characterization:** Powder XRD patterns were measured to examine crystal structures of FMOs using a Rigaku X-ray diffractometer with  $\text{Cu K}\alpha$  radiation ( $\lambda = 1.5418 \text{ \AA}$ ). All the presented XANES spectra at Fe K- and Mn K-edges were collected in transmission mode using the beam line 10C of the Pohang Accelerator Laboratory in Korea. Reference spectra were simultaneously measured using Fe and Mn metal foils for energy calibration.

**Electron Microscopy Characterization:** SEM measurement was performed to investigate the morphology of FMOs using a JEOL JSM-6700F. (S)TEM was conducted to analyze the morphology and crystal structure of FMOs using a JEOL JEM-2100F operated at 200 kV and a 60–300 Titan Themis operated at 300 kV equipped with a Cs corrector for the probe forming lens. The chemical composition of FMOs was analyzed by EDS in the SEM and STEM mode. EELS spectra in STEM were measured using a dual acquisition mode.<sup>[32]</sup> All the EELS spectra were corrected for channel to channel gain variations and dark current, and the backgrounds were removed using a standard power law.<sup>[33]</sup> A double arctangent step function was applied for further post-edge background subtraction of Fe L- and Mn L-edges. The relative amount of Mn and Fe and elemental core loss maps were obtained using HyerSpy.<sup>[34]</sup>

**Electron Tomography:** HAADF-STEM images were obtained from a long CNT region every  $2.5^\circ$  or  $5^\circ$  tilt angle over  $\pm 60^\circ$  range using a 60–300 Titan Themis at 300 kV. The acquired images were aligned using the TomoJ plugin in ImageJ. To reconstruct the 3D volume of the long CNT region, simultaneous iterative reconstruction<sup>[35–37]</sup> and discrete algebraic reconstruction technique were applied.<sup>[38,39]</sup> Finally, reconstructed volume was visualized using a Tomviz software.<sup>[40]</sup>

#### Supporting Information

Supporting Information is available from the Wiley Online Library or from the author.

#### Acknowledgements

J.L. acknowledges financial support from the Alexander von Humboldt Foundation. This work was supported by a National Research Foundation of Korea (NRF) Grant funded by the government of Korea (MSIP) (no. NRF-2020R1A2C3008671) and by the government of Korea (MSIT) (no. NRF-2017R1A5A1015365).

#### Conflict of Interest

The authors declare no conflict of interest.

#### Keywords

2D nanosheets, carbon nanotubes, electron energy loss spectroscopy, electron microscopy, XANES spectroscopy

Received: May 3, 2020  
Published online: July 12, 2020

- [1] V. Georgakilas, J. A. Perman, J. Tucek, R. Zboril, *Chem. Rev.* **2015**, *115*, 4744.
- [2] M. F. L. De Volder, S. H. Tawfik, R. H. Baughman, A. J. Hart, *Science* **2013**, *339*, 535.
- [3] C. T. Wirth, B. C. Bayer, A. D. Gamalski, S. Esconjauregui, R. S. Weatherup, C. Ducati, C. Baehtz, J. Robertson, S. Hofmann, *Chem. Mater.* **2012**, *24*, 4633.
- [4] H. Yoshida, S. Takeda, T. Uchiyama, H. Kohno, Y. Homma, *Nano Lett.* **2008**, *8*, 2082.
- [5] X. Huang, R. Farra, R. Schlögl, M.-G. Willinger, *Nano Lett.* **2019**, *19*, 5380.
- [6] V. Jourdain, C. Bichara, *Carbon* **2013**, *58*, 2.
- [7] Z. He, J.-L. Maurice, A. Gohier, C. S. Lee, D. Pribat, C. S. Cojocaru, *Chem. Mater.* **2011**, *23*, 5379.
- [8] X. Jin, J. Lim, Y. Ha, N. H. Kwon, H. Shin, I. Y. Kim, N.-S. Lee, M. H. Kim, H. Kim, S.-J. Hwang, *Nanoscale* **2017**, *9*, 12416.
- [9] Y. Y. Wei, G. Eres, V. I. Merkulov, D. H. Lowndes, *Appl. Phys. Lett.* **2001**, *78*, 1394.



- [10] S. Rai, A. Ikram, S. Sahai, S. Dass, R. Shrivastav, V. R. Satsangi, *Int. J. Hydrogen Energy* **2017**, *42*, 3994.
- [11] J. Wu, Z. Lan, J. Lin, M. Huang, Y. Huang, L. Fan, G. Luo, Y. Lin, Y. Xie, Y. Wei, *Chem. Soc. Rev.* **2017**, *46*, 5975.
- [12] Q. Gao, Q. Liu, M. Li, X. Li, Y. Liu, C. Song, J. Wang, J. Liu, G. Shen, G. Han, *Thin Solid Films* **2013**, *544*, 357.
- [13] J. Yang, W. Liu, L. Dong, Y. Li, C. Li, H. Zhao, *Appl. Surf. Sci.* **2011**, *257*, 10499.
- [14] J. Lim, J. M. Lee, B. Park, X. Jin, S.-J. Hwang, *Nanoscale* **2017**, *9*, 792.
- [15] S.-J. Hwang, H. S. Park, J.-H. Choy, G. Campet, *J. Phys. Chem. B* **2000**, *104*, 7612.
- [16] L. A. Grunes, *Phys. Rev. B* **1983**, *27*, 2111.
- [17] N. Treuil, C. Labrugère, M. Menetrier, J. Portier, G. Campet, A. Deshayes, J.-C. Frison, S.-J. Hwang, S.-W. Song, J.-H. Choy, *J. Phys. Chem. B* **1999**, *103*, 2100.
- [18] T. W. Kim, H.-W. Ha, M.-J. Paek, S.-H. Hyun, I.-H. Baek, J.-H. Choy, S.-J. Hwang, *J. Phys. Chem. C* **2008**, *112*, 14853.
- [19] S.-J. Hwang, H.-S. Park, J.-H. Choy, G. Campet, *Chem. Mater.* **2000**, *12*, 1818.
- [20] A. Gohier, C. P. Ewels, T. M. Minea, M. A. Djouadi, *Carbon* **2008**, *46*, 1331.
- [21] P. A. van Aken, B. Liebscher, V. J. Styrsa, *Phys. Chem. Miner.* **1998**, *25*, 323.
- [22] H. Tan, J. Verbeeck, A. Abakumov, G. Van Tendeloo, *Ultramicroscopy* **2012**, *116*, 24.
- [23] L. P. Keller, *Meteorit. Planet. Sci.* **1998**, *33*, 913.
- [24] L. A. Grunes, R. D. Leapman, C. N. Wilker, R. Hoffmann, A. B. Kunz, *Phys. Rev. B* **1982**, *25*, 7157.
- [25] Y. Jin, H. Xu, A. K. Datye, *Microsc. Microanal.* **2006**, *12*, 124.
- [26] M.-C. Lee, G. Simkovich, *Metall. Trans. A* **1988**, *19*, 2115.
- [27] C.-P. Yap, C. L. Liu, *Trans. Faraday Soc.* **1932**, *28*, 788.
- [28] Y. Yin, R. M. Rioux, C. K. Erdonmez, S. Hughes, G. A. Somorjai, A. P. Alivisatos, *Science* **2004**, *304*, 711.
- [29] S. R. Shatynski, *Oxid. Met.* **1979**, *13*, 105.
- [30] T. I. A. Kosolapova, *Carbides: Properties, Production, and Applications*, Plenum Press, New York **1971**.
- [31] K. Kai, Y. Yoshida, H. Kageyama, G. Saito, T. Ishigaki, Y. Furukawa, J. Kawamata, *J. Am. Chem. Soc.* **2008**, *130*, 15938.
- [32] J. Scott, P. J. Thomas, M. MacKenzie, S. McFadzean, J. Wilbrink, A. J. Craven, W. A. P. Nicholson, *Ultramicroscopy* **2008**, *108*, 1586.
- [33] R. F. Egerton, *Rep. Prog. Phys.* **2009**, *72*, 016502.
- [34] F. de la Peña, E. Prestat, V. T. Fauske, P. Burdet, P. Jokubauskas, M. Nord, T. Ostasevicius, K. E. MacArthur, M. Sarahan, D. N. Johnstone, J. Taillon, J. Lähnemann, V. Migunov, A. Eljarrat, J. Caron, T. Aarholt, S. Mazzucco, M. Walls, T. Slater, F. Winkler, B. Martineau, G. Donval, R. McLeod, E. R. Hoglund, I. Alxneit, D. Lundeby, T. Henninen, L. F. Zagonel, A. Garmannslund, hyperspy/hyperspy: HyperSpy v1.5.2, Zenodo, **2019**. <http://doi.org/10.5281/zenodo.3396791>
- [35] P. Gilbert, *J. Theor. Biol.* **1972**, *36*, 105.
- [36] A. V. Lakshminarayanan, A. Lent, *J. Theor. Biol.* **1979**, *76*, 267.
- [37] G. Haberkorn, A. Orthacker, M. Albu, J. Li, G. Kothleitner, *Nanoscale* **2014**, *6*, 14563.
- [38] K. J. Batenburg, S. Bals, J. Sijbers, C. Kübel, P. A. Midgley, J. C. Hernandez, U. Kaiser, E. R. Encina, E. A. Coronado, G. Van Tendeloo, *Ultramicroscopy* **2009**, *109*, 730.
- [39] A. Zürner, M. Döblinger, V. Cauda, R. Wei, T. Bein, *Ultramicroscopy* **2012**, *115*, 41.
- [40] B. D. A. Levin, E. Padgett, C.-C. Chen, M. C. Scott, R. Xu, W. Theis, Y. Jiang, Y. Yang, C. Ophus, H. Zhang, D.-H. Ha, D. Wang, Y. Yu, H. D. Abruña, R. D. Robinson, P. Ercius, L. F. Kourkoutis, J. Miao, D. A. Muller, R. Hovden, *Sci. Data* **2016**, *3*, 160041.